RESEARCH ARTICLE

g-C$_3$N$_4$/graphene oxide/SnFe$_2$O$_4$ ternary composite for the effective sunlight-driven photocatalytic degradation of methylene blue

Suman Tahir[1] · Muhammad Zahid[1] · Muhammad Asif Hanif[1] · Muhammad Yasir Javed[2]

Abstract

A broadly used dye, methylene blue (MB), adversely impacts human health and water resources, which triggers efficient methods for its elimination. Semiconductor-based heterogeneous photocatalysis is an environmentally friendly approach that effectively degrades organic pollutants. The purpose of the current work is to elucidate and validate the application of a promising g-C$_3$N$_4$/GO/SnFe$_2$O$_4$ (CGS) composite for the environmental remediation of methylene blue dye. The ternary CGS composite has been synthesized using a solvothermal approach. The fabricated composites were analyzed through FTIR, XRD, SEM/EDX, UV–VIS spectroscopy, TEM, and XPS. The photoactivity of composites and affecting parameters (pH, H$_2$O$_2$ dosage, composite amount, initial dye concentration, and irradiation time) were observed in sunlight illumination. The optimal conditions for photocatalytic degradation were pH = 5, photocatalyst dosage = 30 mg/100 mL, H$_2$O$_2$ dosage = 6 mM, and initial dye concentration (IDC) of 10 ppm employing ternary CGS composite, and MB dye was degraded effectively within 1 h. Ninety-eight percent degradation efficacy was attained by employing ternary CGS composite under the optimized conditions. Scavenging analysis suggested that $^{\bullet}$OH radicals were the key reactive oxygen species (ROS) responsible for the photodegradation of MB dye. Furthermore, the CGS nanocomposite exhibited outstanding recyclability of 84% after five consecutive runs, demonstrating its potential for use in practical applications, particularly pollutant removal.

Keywords Wastewater treatment · Heterogeneous photocatalysis · Metal ferrite · Heterojunction · Graphene oxide · Photodegradation

Introduction

With the rapid population growth and industrialization, environmental issues and energy shortages are getting increasingly worse worldwide (Zhang et al. 2019). A larger quantity of various pollutants such as pesticides, dyes, heavy metals, personal care products, and pharmaceuticals, are inevitably discharged into natural aquatic bodies mainly from the industrial sector which causes a great threat to human health and ecological systems (Wacławek et al. 2017). Synthetic organic dyes are harmful contaminants, participating in up

to 0.7 million tons of worldwide annual production (Martínez-Huitle and Brillas 2009). The food, textile, cosmetics, electronic, hair color, and leather industrial units have raised approximately 0.28 million tons of organic dyestuff worldwide (Solís et al. 2012). Dyes inhibit aquatic photosynthetic activity and reduce dissolved oxygen, leading to toxicity to fauna, flora, and human beings. Methylene blue, commonly termed MB, is a cationic, water-soluble dye utilized to dye wool, silk, cotton, jute, and plastic (Ma et al. 2009). MB has numerous hazardous effects on human beings, like vomiting, increased heartbeat, cyanosis, jaundice, and tissue necrosis, and poses a risk to the environment as well (Zhan et al. 2015).

Since dyes are toxic and comparatively resistant to degradation by conventional wastewater remediation processes, hence advanced oxidation processes (AOPs), green technology is the suitable approach (Pooladi and Bazargan-Lari 2023). Because of the robust mineralization capability, AOPs are extremely appealing for practical implementation, typically arising from generated ROS such as $^{\bullet}$OH, $^{\bullet}$HO$_2$,

✉ Muhammad Zahid
 rmzahid@uaf.edu.pk

1 Department of Chemistry, University of Agriculture, Faisalabad 38040, Pakistan

2 Department of Physics, University of Agriculture, Faisalabad 38040, Pakistan

and $\cdot O_2^-$ (Miklos et al. 2018). In AOPs, $\cdot OH$ radicals are extremely reactive species and are produced in situ that induce non-selective oxidation of organic contaminants to H_2O, CO_2, and particular inorganic ions. Semiconductor-based heterogeneous photocatalysis is a promising technology among AOPs which is believed to be an outstanding solar energy transformation operating at ambient temperature and pressure in the field of pollutant elimination (Bambaeero and Bazargan-Lari 2021).

Graphitic carbon nitride (g-C_3N_4), a metal-free 2D polymeric semiconductor, has achieved huge attraction due to its interesting inherent properties, such as low cost, simple synthesis, tunable electronic structure, suitable band gap, high elemental abundance, ecofriendly nature, and superior thermal and chemical stabilities (Fu et al. 2018). g-C_3N_4 has extensively been explored for the degradation of recalcitrant contaminants in visible light owing to its moderate band gap ranging between 2.4 and 2.8 eV (Kong et al. 2016). Though, due to quick recombination rate of photoinduced e^-/h^+ pair, photoactivity of g-C_3N_4 is limited (Schwinghammer et al. 2014). Numerous g-C_3N_4-based heterojunctions, for example, g-C_3N_4/GO (Wan et al. 2016), g-C_3N_4/CeVO$_4$ (Ren et al. 2016), Bi_2O_3/g-C_3N_4 (He et al. 2018), g-C_3N_4/WO$_3$ (Yu et al. 2017), and CuInS$_2$/g-C_3N_4 (Guo et al. 2019) with remarkably improved photocatalytic activity, have been reported which reduces the rate of e^-/h^+ pairs. However, recycling and separation of catalysts is a significant task for their utilization in wastewater treatment.

Moreover, the coupling of g-C_3N_4 with metal ferrites (M-Fe_2O_4, M = Mn, Zn, Co, Cu) has been established not merely to enhance photocatalytic activity but also ease to magnetically recycle the photocatalyst (Chen et al. 2016). Based on the comparison with other M-Fe_2O_4, $SnFe_2O_4$ can be deemed as a best option, due to its non-toxic, magnetic behavior and plenty of Fe and Sn elements on the globe (Rai et al. 2015). Owing to the attractive properties of $SnFe_2O_4$, it is employed in numerous applications like hydrogen production (Jo et al. 2020), photocatalytic CO_2 reduction (Jia et al. 2020), potentiometric nonenzymatic H_2O_2 sensor (Bindu et al. 2016), lithium-ion batteries (Zhang et al. 2021), and photodegradation of dyes (Jia et al. 2017). Also, the reported band gap of $SnFe_2O_4$ is 2.53 eV, which is highly efficient for the photocatalytic degradation of recalcitrant contaminants because of its absorption in the visible light region (Chen et al. 2016).

Currently, Z-scheme-based photocatalysts have been fabricated for enhanced redox capability and charge carrier separation efficacy during photocatalytic reactions (Fu et al. 2019). To improve the efficiency of the electron relay, it is essential to introduce an electron mediator between two semiconductors in the Z-scheme photosystem (Liu et al. 2018). GO is one of the efficient electron mediators because of its effective electron transferring mobility achieving up to

200,000 cm^2 V^{-1} S^{-1}, unique mechanical strength, stability, and biocompatibility (Gebreslassie et al. 2019). Graphene oxide (GO) is a single-atom-thick and 2D carbon-based nanomaterial that is organized in a hexagonal matrix (Tahir et al. 2022). GO has a higher capability to trap electrons from semiconductor photocatalysts and improves photoactivity due to its higher specific surface area and excellent electrical, and thermal features (Wu et al. 2018). Lu and his colleagues reported Z-scheme composite g-C_3N_4/rGO/WO$_3$ with rGO as an electron facilitator between g-C_3N_4 and WO$_3$ for degradation of ciprofloxacin (Lu et al. 2019). The g-C_3N_4/rGO/WO$_3$ nanocomposite displays a 2 times higher degradation efficiency than binary g-C_3N_4/WO$_3$. To the best of our knowledge, g-C_3N_4/GO/$SnFe_2O_4$ composite has not been reported.

In the present study, we report the g-C_3N_4/GO/$SnFe_2O_4$ (CGS) ternary composite, where g-C_3N_4/$SnFe_2O_4$ as photocatalysts and GO as electron mediator was employed. The in situ solvothermal method was used for the synthesis of a novel CGS composite and was utilized for the MB dye degradation in sunlight. The analysis of synthesized composites using XRD, XPS, SEM/EDX, FTIR, UV–Vis spectroscopy, and TEM/HR-TEM was employed to explore the crystalline structure, chemical composition, morphology, purity, functional group, and optical features of the prepared samples. The study showed that GO-supported g-C_3N_4/$SnFe_2O_4$ provides improved surface area and photoinduced charge carrier separation, which efficiently increases photocatalyst visible light behavior.

Materials and methods

Chemicals

All the chemicals and reagents employed in the present work were of analytical grade. Ethylene glycol (99.8%), hydrochloric acid (HCl, 35% w/w), sodium hydroxide (NaOH pellets, 98%), potassium permanganate (KMNO$_4$, 99%), sodium nitrate (NaNO$_3$, 98%), hydrogen peroxide (H$_2O_2$; 35% w/w), and sulfuric acid (H$_2SO_4$, 98%) were attained from Sigma-Aldrich. Graphite powder (99%) from Scharlau, ethanol (C$_2$H$_5$OH, 95.6%) from Merck, and melamine (C$_3$N$_3$(NH$_2$)$_3$), 99%) was obtained from DAEJUNG. Tin chloride (SnCl$_2$, 99%) and iron (II) chloride tetrahydrate (FeCl$_2$•4H$_2$O, 99%) were obtained from Glentham Life Sciences. Distilled water was utilized during the research work.

Preparation of GO

Using modified Hummers method, GO was prepared, which was earlier described in our study (Tabasum et al. 2018). Sodium nitrate (2.5 g) and graphite (5 g) were

combined in an Erlenmeyer flask, and dropwise, sulfuric acid was added with continuous stirring. Then, 30 g of KMnO$_4$ was gradually added to above mixture by maintaining the temperature of reaction mixture near 0 °C. After that, the solution was diluted with distilled water keeping the temperature at 90 °C. After centrifugation, the pH of obtained suspension was neutralized. The thick dark brown paste was sonicated to obtain the GO layers and followed by drying in an electric-oven at 70 °C. The incorporation of oxygenated groups in GO by modified Hummers method using graphite is shown in Fig. 1.

Preparation of g-C$_3$N$_4$

g-C$_3$N$_4$ was prepared through a thermal polymerization approach (Saher et al. 2021). Ten grams of melamine was taken in the crucible and then placed in a muffle furnace for 3 h at 550 °C with a ramping rate of 5 °C/min. Then, the yellow-colored g-C$_3$N$_4$ was obtained. Figure 1 shows the structural transformation involved during the synthesis of g-C$_3$N$_4$ using melamine (Sudhaik et al. 2018).

Synthesis of g-C$_3$N$_4$/SnFe$_2$O$_4$ composite (CS)

g-C$_3$N$_4$/SnFe$_2$O$_4$ (CS) binary composite was synthesized by in situ solvothermal method (Jia et al. 2020). The precursors of metal ferrite such as iron salt FeCl$_2$•4H$_2$O (3.4 mmol) and metal salt SnCl$_2$ (1.7 mmol) were dissolved in 50 mL ethylene glycol with constant stirring. Afterwards, 0.2 g of g-C$_3$N$_4$ was dispersed in 50 mL distilled water and subjected to ultrasonic irradiation for 20 min was added into the above mixture. Then, slowly, 3M NaOH was added to maintain the pH of the mixture at 10. After that pour, the mixture into an autoclave lined with Teflon covering for 15 h at 200 °C and subsequently naturally cool down. The resultant slurry was rinsed with ethanol and deionized water and followed by drying in an oven at 70 °C.

Synthesis of GO/SnFe$_2$O$_4$ composite (GS)

GO/SnFe$_2$O$_4$ (GS) binary composite was synthesized by in situ solvothermal method. SnCl$_2$ (1.7 mmol) and FeCl$_2$•4H$_2$O (3.4 mmol) dissolved in the 50 mL ethylene glycol were stirred for 60 min. Then, 0.2 g of GO was dispersed in 50 mL distilled water subjected to ultrasonic
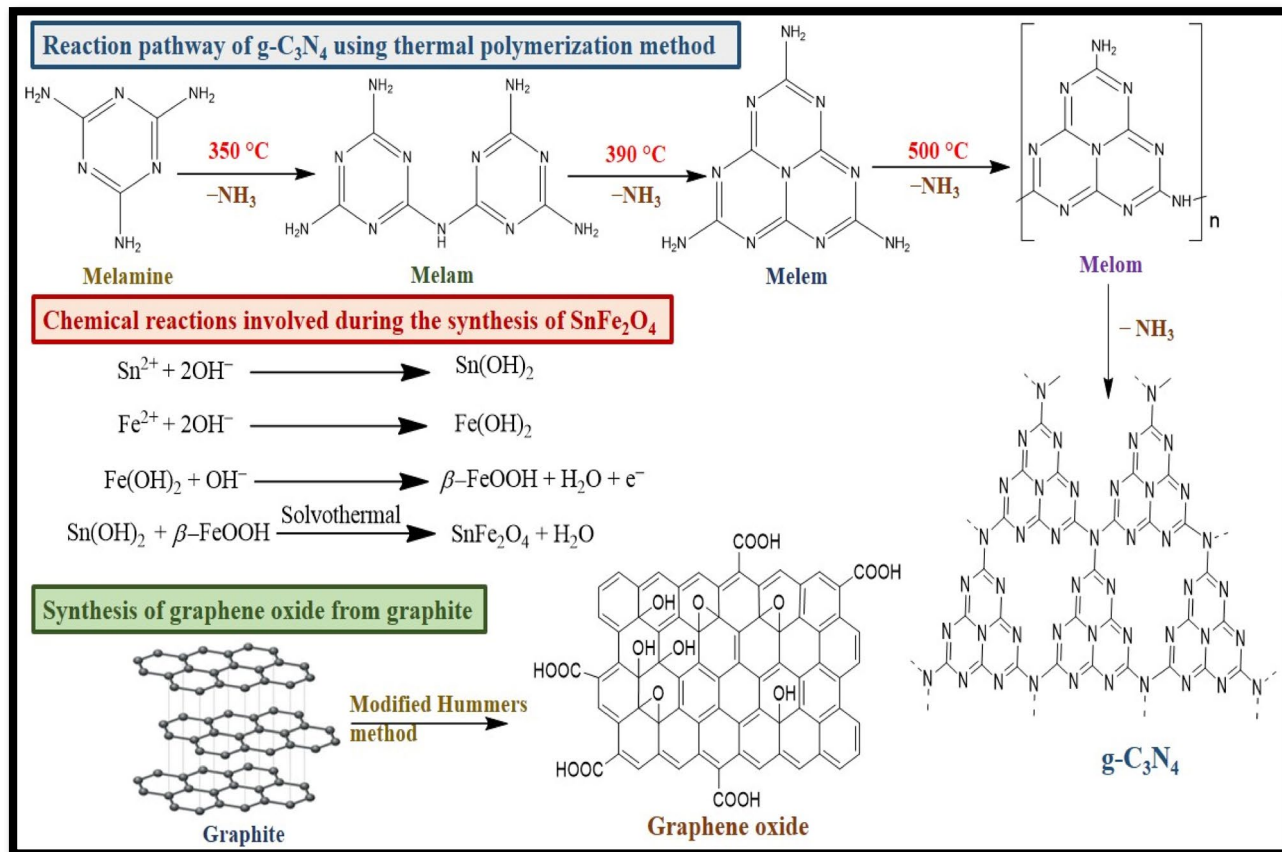

Fig. 1 Reactions involved during the synthesis of g-C$_3$N$_4$/GO/SnFe$_2$O$_4$ (CGS) composite

irradiation for 20 min and introduced into the above mixture. Afterwards, 3M NaOH was slowly added, and the pH of the mixture was maintained at 10. Then, pour the mixture into an autoclave for 15 h at 180 °C and subsequently naturally cool down. The resultant product was rinsed with distilled water and ethanol and then oven-dried at 60 °C (Jia et al. 2017).

Synthesis of ternary g-C$_3$N$_4$/GO/SnFe$_2$O$_4$ (CGS)

CGS ternary composite was synthesized by the in situ solvothermal method. In a usual method, (3.4 mmol) SnCl$_2$ and (6.8 mmol) FeCl$_2$•4H$_2$O dissolved in the 50 mL ethylene glycol were stirred for 60 min. Then, 30 wt% (0.3 g) of g-C$_3$N$_4$ and 20 wt% (0.2 g) of GO were separately dispersed in 50 mL distilled water and subjected to ultrasonic radiation for 20 min. Afterwards, 3M NaOH was slowly added, and the pH of the mixture was adjusted to 10. Then, pour mixture into an autoclave lined with Teflon covering at 180 °C for 12 h and consequently naturally cool down. The resultant product was rinsed with ethanol and distilled water and then oven-dried at 60 °C and labelled as CGS. The obtained product was ground and transformed into powder form for further use. The schematic diagram for the fabrication of CGS composite using the solvothermal method is shown in Fig. S1. The chemical reactions involved in the formation of SnFe$_2$O$_4$ NPs in CGS composite are presented in Fig. 1 (Jia et al. 2017).

Characterization and equipment

The as-synthesized binary and ternary composites were analyzed through various techniques. Crystalline and phase study of synthesized composites was done employing an X-ray diffractometer (Bruker D8-Advanced equipment) provided with Cu-Kα radiation over a range of 2θ values from 5 to 80°. X-ray photoelectron spectroscopy (XPS) was used for the evaluation of surface chemical composition and elemental analysis. Surface morphology of composites was established utilizing scanning electron microscopy (SEM) coupled with EDS for the identification of elemental composition of composites. Functional group detection of composites was performed employing Fourier-transform infrared spectroscopy. The assessment of percentage degradation and band gap evaluation was done by UV-visible spectroscopy (CECIL CE 7200). HR-TEM analysis was employed for surface morphologies (HR-TEM, JEOL-JEM 100CX).

Estimation of photodegradation experiment

The photodegradation experiments of MB dye were performed in sunlight utilizing binary GS, CS, and ternary CGS composites for 1 h. Figure S2 shows the schematic diagram of a sunlight-driven photodegradation experiment using photocatalysts. The impact of numerous parameters comprising composite dose (10–100 mg/100 mL), pH (2–9), IDC (2–20 ppm), oxidant dose (2–20 mM), and contact time (10–60 min) was observed. In the present work, MB was chosen as a model pollutant. Using a pH meter, 0.1 M solutions of NaOH and HCl were utilized to maintain the pH of MB dye solutions. The desirable amount of photocatalysts was dispersed in 10 ppm MB dye having 100 mL solution and subjected to ultrasonication for approx. 2–3 min. After sonicating MB dye solutions, beakers were kept in dark for approx. 30 min, to attain adsorption-desorption equilibrium phase between catalyst surface and MB dye molecules. Then, H$_2$O$_2$ in a particular concentration was added to the reaction mixture. Under sunlight, MB solutions were placed for 1 h at 180 rpm in an electrical orbital shaker (Pamico Technologies). Using an external magnet, a composite was separated from the MB solution, and absorbance was estimated by employing a UV-visible spectrophotometer at 664 nm. Percentage degradation was evaluated, afterwards comparing the absorbance of untreated and treated MB dye solutions. The % degradation was evaluated employing the formula given in Eq. (1).

$$Degradation(\%) = 1 - \frac{A}{A_o} \times 100 \qquad (1)$$

Herein, initial absorbance is denoted as A_o and A is absorbance afterwards degradation under sunlight. The sunlight intensity and the brightness were measured employing a solar power meter and a light meter.

Characterization of synthesized composites

FTIR analysis

For detecting the functional group of the prepared GS, CS, and CGS composites, FTIR analysis was carried out. Figure 2a displays FTIR spectrum of binary CS composite and shows that a peak at 810 cm^{-1} was ascribed to triazine units. The band peaks ranging between 1200 and 1600 cm^{-1} are linked to stretching vibrations of C–N and C=N, which confirm the presence of g-C$_3$N$_4$ (Zhang et al. 2018). The band ranging from 2950 to 3386 cm^{-1} indicates the occurrence of uncondensed -NH$_2$ and -NH groups. The lower intensity g-C$_3$N$_4$ peaks in CS composite may be because of the consumption of g-C$_3$N$_4$ by reacting with OH$^-$ during the solvothermal method. The representative absorption peaks at 574 and 640 cm^{-1} were because of Fe-O and Sn-O vibrations, supporting the existence of SnFe$_2$O$_4$ (Xu et al. 2017). Furthermore, all peaks of g-C$_3$N$_4$ and SnFe$_2$O$_4$ were displayed

Fig. 2 FTIR spectra of binary and ternary composites **a** CS, **b** GS, and **c** CGS
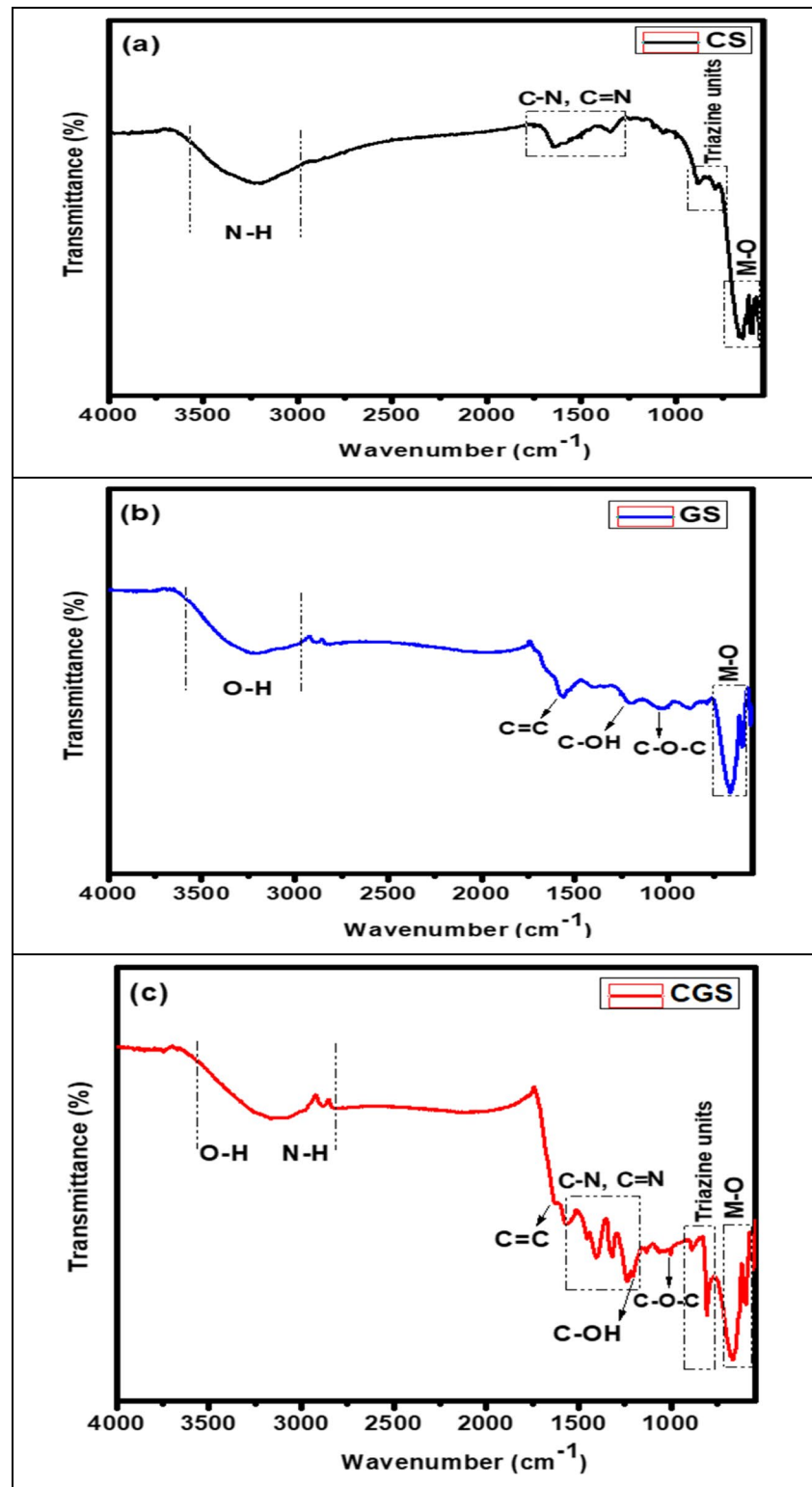
in the CS nanocomposite, which showed the effective preparation of binary composite.

FTIR spectrum of binary GS composite shows the peaks of GO at 1038 (C-O-C), 1215 (C–OH), and 1645 cm^{-1} (C=C) groups, in Fig. 2b (Ossonon and Bélanger 2017).

The band is approx. 3100–3500 cm^{-1} which might be attributed to adsorbed H$_2$O molecule vibrations. The peaks at 565 and 630 cm^{-1} noticed for SnFe$_2$O$_4$ were because of Fe-O and Sn-O vibrations (Cai et al. 2016). Hence, it verifies the concurrence of SnFe$_2$O$_4$ NPs on the GO sheets.

FTIR spectrum of ternary CGS composite presented a minor peak at 569 cm^{-1} ascribed to Fe-O while an intensive peak at 635 cm^{-1} ascribed to Sn-O vibration, which verifies the presence of $SnFe_2O_4$ (Fig. 2c) (Lee and Lu 2015). The peak at about 807 cm^{-1} is responsible for the tris-s-triazine unit, which strongly supports the formation of g-C_3N_4 (Deng et al. 2017). The various peaks at 1233, 1318, and 1410 cm^{-1} are credited to C-N stretching, and the peak at 1559 cm^{-1} belongs to C=N vibrations (Gebreslassie et al. 2019). For the GO, the peaks occur at 1050 cm^{-1} (C-O-C), 1210 (C-OH), 1626 cm^{-1} (C=C), and 3315 cm^{-1} (-OH) groups, respectively (Hu et al. 2019). The presence of numerous oxygenated functional groups on GO nanosheet shows that graphite was well oxidized to GO (Singh et al. 2017). All distinctive peaks of GO, g-C_3N_4, and $SnFe_2O_4$ were found in novel ternary CGS nanocomposite and suggest that $SnFe_2O_4$ is successfully bonded to the g-C_3N_4 and GO.

XRD analysis

The crystalline structure of synthesized nanocomposites was investigated using XRD in 2θ range of 5–80°. Figure 3 presents the XRD patterns of binary composites, namely, GS and CS, and ternary CGS nanocomposites. XRD pattern of the binary CS composite showed various intense diffraction 2θ angles at 18.1°, 30.7°, 35.3°, 43.1°, 52.5°, 56.8, and 62.3° corresponding to the (111), (220), (311), (400), (422), (511), and (440) planes of the $SnFe_2O_4$. The typical peak at $2\theta = 27.3°$, which is indexed to (002) diffraction plane of g-C_3N_4 (Borthakur and Saikia 2019). XRD pattern of binary GS composite shows evident diffraction peaks of $SnFe_2O_4$ and GO. The diffraction peak of GO (002) is observed at 26.3° (Ahmad et al. 2021). This shows that during the solvothermal method, GO was reduced into graphene

(Fu et al. 2012). The diffraction peaks positioned at 18.5°, 30.5°, 35.7°, 42.6°, 53.1°, 56.6, and 62.8°, corresponding to the (111), (220), (311), (400), (422), (511), and (440) planes of the $SnFe_2O_4$. The lack of other diffraction peaks proves the higher purity of the nanocomposite without any noticeable by-products.

The ternary CGS nanocomposite displays the diffraction peak of g-C_3N_4 at 27.1° which corresponds to the (002) plane (JCPDS card no. 87-1526) (Jia et al. 2017). This is related to the in-planar arrangement of conjugated aromatic networks (Jo et al. 2020), while the peak at 13.1° for (001) diffraction plane of GO relates to the incorporation of oxygen-containing groups on graphite sheets (Paulchamy et al. 2015). The $SnFe_2O_4$ displayed various diffraction 2θ angles at 18.3°, 30.2°, 35.5°,37.1°, 42.9°, 53.4°, 57.1, 62.5°, and 74.1° corresponding to the (111), (220), (311), (222), (400), (422), (511), (440), and (533) planes of the $SnFe_2O_4$, that was well-suited with JCPDS Card No. 71-0694 (Zhang et al. 2021). XRD of synthesized novel CGS composite shows peaks attributable to GO, g-C_3N_4 and $SnFe_2O_4$, demonstrating the successful formation of ternary composite. No considerable diffraction peaks of any impurities were noticed in g-C_3N_4/GO/$SnFe_2O_4$ composite, demonstrating that the synthesized composite is pure. Using Debye-Scherrer formulae equation, average particle size was calculated.

$$D = K\lambda/\beta\cos\theta \tag{2}$$

D is crystallite size, λ is the wavelength of CuKα (0.154 nm), β is associated with FWHM of photocatalysts, θ refers to the diffraction angle, and Scherrer constant K with 0.94 value. Average crystallite sizes for CS, GS, and CGS nanocomposites were discovered to be 38, 45, and 28 nm, respectively.
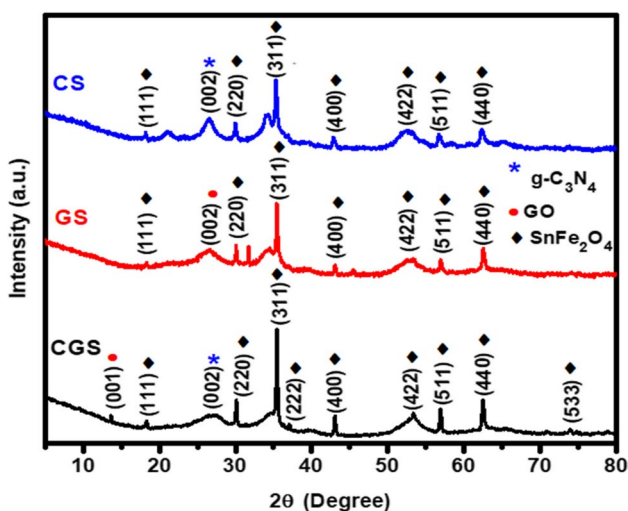
SEM/EDX analysis

The morphologies of GS, CS, and CGS composites were noticed by SEM, and images are presented in Fig. 4. In Fig. 4a, $SnFe_2O_4$ NPs were well scattered and anchored on g-C_3N_4 nanosheets (Jia et al. 2017). The graphene oxide looked like a sheet, while the $SnFe_2O_4$ nanoparticles were seen as spherical shapes as established in Fig. 4c. It is apparent from Fig. 4c that SEM micrographs of GS composite that aggregated spherical-shaped $SnFe_2O_4$ nanoparticles were dispersed on GO sheets, which can be ascribed to fabrication of binary composite by immobilization (Akhundi and Habibi-Yangjeh 2016). Graphene oxide is comprised of large sheets having a paper-like configuration with thin layers, which certainly offer an adequate surface area for the $SnFe_2O_4$ NPs to be loaded, as seen in Fig. 4e. The aggregated $SnFe_2O_4$ NPs with various cluster sizes and GO sheet morphology and g-C_3N_4 were well-preserved on novel

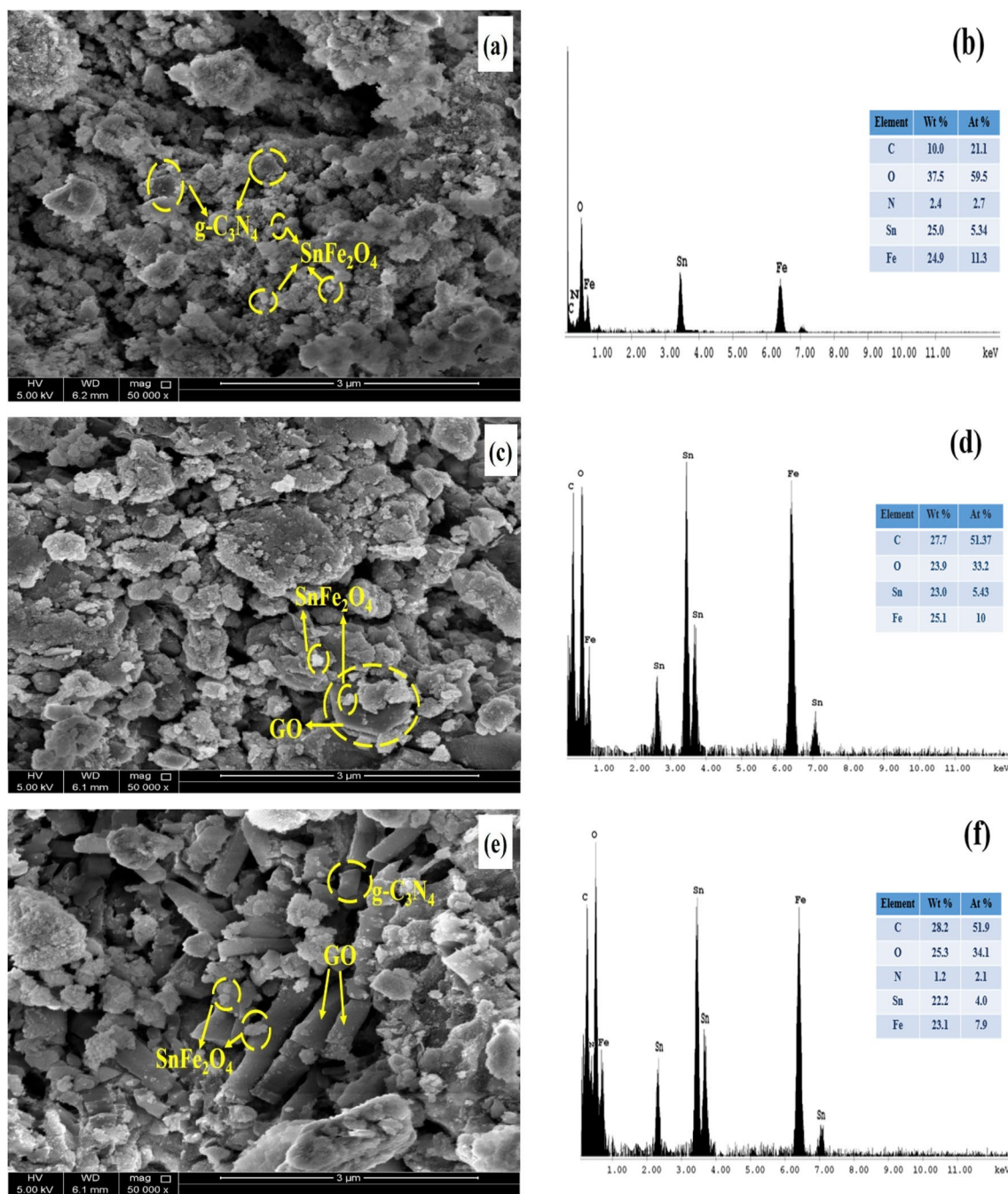**Fig. 3** XRD pattern of GS, CS, and CGS composites

Fig. 4 SEM/EDX analysis of CS (**a**, **b**), GS (**c**, **d**), and CGS (**e**, **f**) composites

ternary CGS composite. There is a morphological alteration among CS, GS, and CGS in which ternary CGS composite comprises both spherical particles of $SnFe_2O_4$ and nanosheets of GO and g-C_3N_4.

EDS analysis was used to investigate the elemental configuration and purity of the binary and ternary nanocomposites. The formation of a novel ternary CGS composite was verified through EDX study as well, which confirmed the presence of Fe, Sn, C, O, and N in prepared sample (Fig. 4f).

The atomic weight percentage of CGS composite shows that it is composed of Fe (23.1%), O (25.3%), C (28.2.59%), Sn (22.2%), and N (1.2%). Hence, it can be concluded that the CGS composite is prepared without impurities.

TEM and HR-TEM analysis

The morphological and crystallographic features of prepared binary and ternary nanocomposites were characterized using

TEM and HR-TEM analysis. Figure 5a TEM analysis of CGS shows the existence of a ternary heterojunction interface with very small $SnFe_2O_4$ nanoparticles forming an intricate pattern, randomly dispersed over wrinkled layer structures of $g\text{-}C_3N_4\text{-}GO$. Both $g\text{-}C_3N_4$ and GO are tiny-layered structures made up of graphitic planes having conjugated aromatic structures. Several small depositions of $g\text{-}C_3N_4$ structures, with layers stacked over each, are evident from TEM analysis. The single-layered GO sheets with enhanced surface area are present at the edges in ternary CGS as well
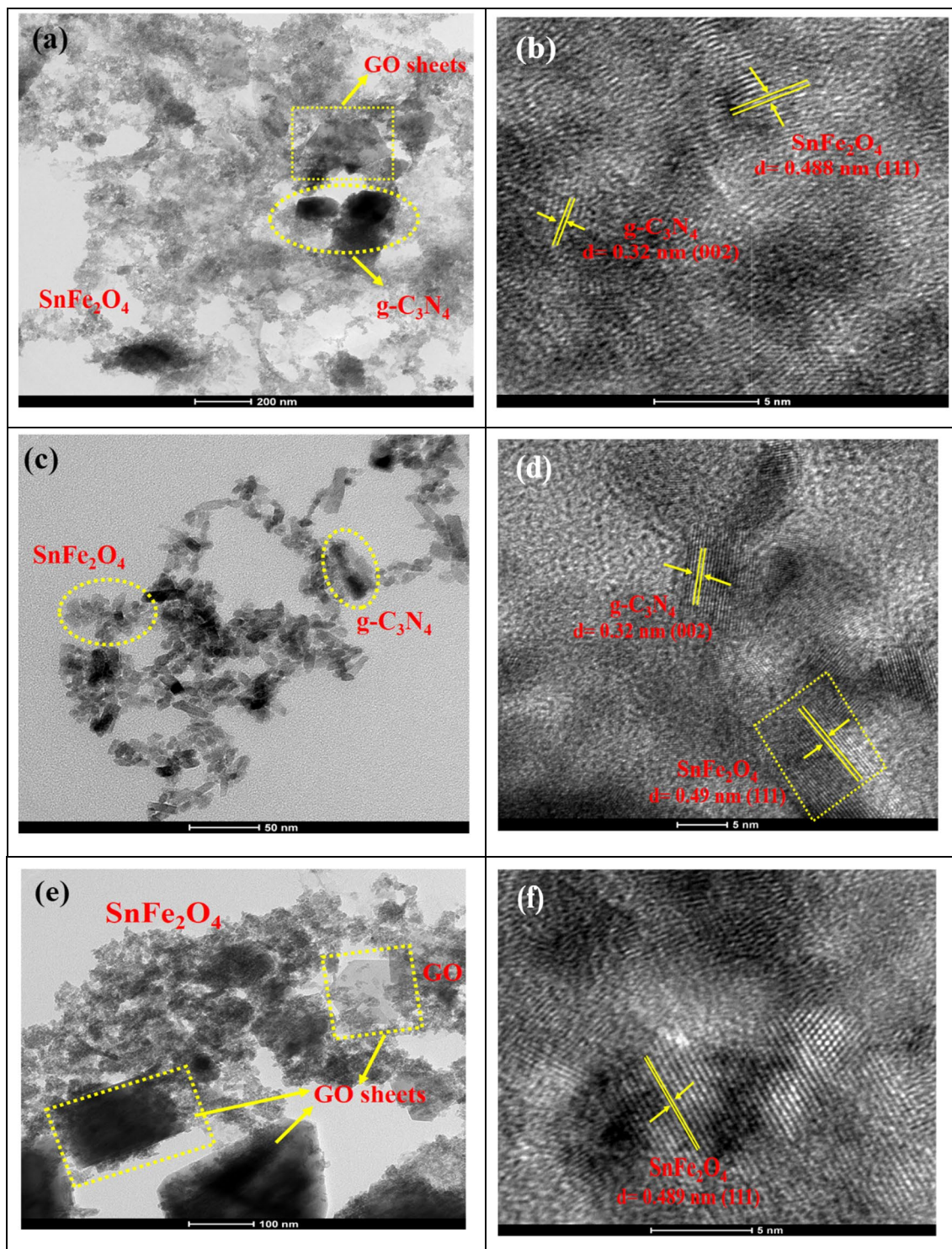

Fig. 5 TEM and HR-TEM micrographs of **a**, **b** CGS, **c**, **d** CS, and **e**, **f** GS

as in binary nanocomposite GS (Fig. 5e), providing more adsorption sites and hence enhanced charge separation by ternary CGS composite. In Fig. 5b, the HR-TEM analysis of CGS shows lattice fringes with (002) and (111) planes of $SnFe_2O_4$ and g-C_3N_4 having interplanar distances of (0.32 nm) and (0.488 nm), well-matched by the earlier reports (Jia et al. 2020). The obvious lattice fringes with an interplanar spacing of 0.49 and 0.32 nm are assigned to the (111) of $SnFe_2O_4$ and (002) of g-C_3N_4 in CS composite (Fig. 5d), and lattice fringes of GS composite with an interplanar spacing of 0.489 nm to the (111) plane of $SnFe_2O_4$ (Fig. 5f). The SAED patterns of ternary and binary nanocomposites in Fig. S3 show bright diffraction rings indicating the polycrystalline nature of all synthesized nanocomposites. The bright rings of ternary CGS are indexed to planes (400), (111), and (220) of $SnFe_2O_4$ and (002) plane of g-C_3N_4 shown in Fig. S3 (a). The ternary CGS nanocomposite shows all components in comparison with binary composites. Hence, the results of FTIR, XRD, SEM, and TEM proved the successful synthesis of CGS composite through the solvothermal method.
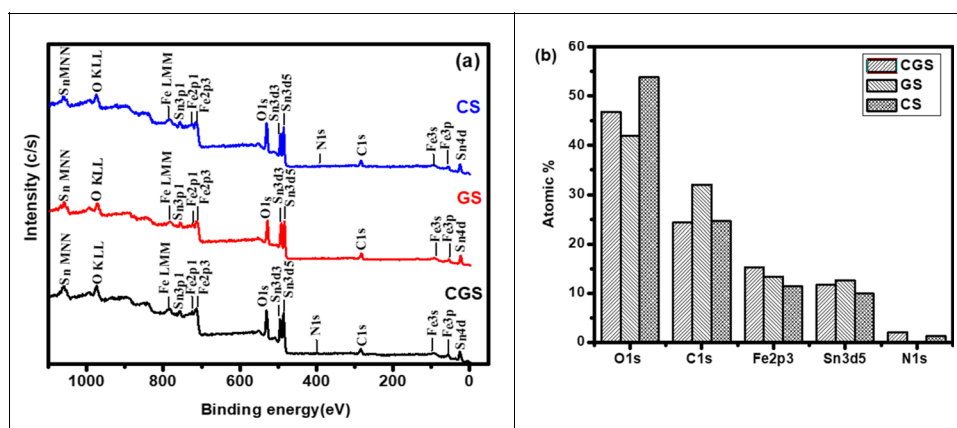
XPS analysis

XPS analysis was performed to observe surface chemical state of elements and atomic weight percentages of ternary CGS, and binary CS, and GS composites in Fig. 6. The signals of Sn 3d5 (486 eV), Fe 2p3 (712.3 eV), O 1s (532.5 eV), N 1s (400.1 eV), and C 1s (287.4 eV) were identified from the survey scan of binary CS composite as shown in Fig. 6a, and no apparent peaks of additional elements were noticed. The binding energy peaks are well-matched with the previous studies (Jia et al. 2020). Figure 6b shows atomic percentages of identified elements such as C 1s, O1s, Sn 3d5, N 1s, and Fe 2p3 which reveals the successful synthesis of CS. XPS analysis of the binary GS composite shows that the signals of Sn 3d5 (485.5 eV), Fe 2p3 (711.1 eV), O 1s (531.5 eV), and C 1s (285.1

eV) were identified from the survey scan of GS (Fig. 6a), which was well matched with previous studies (Xu et al. 2017). The high-resolution XPS spectra of binary GS and CS composites are presented in Figs. S4 and S5.

The survey scan of ternary CGS composite in Fig. 6a shows five various obvious binding energy peaks at 285, 401, 485, 530.7, and 710 eV which show the existence of C, N, Sn, O, and Fe elements. As reported, chief elements of graphene oxide are carbon and oxygen (Hu et al. 2016). Thus, carbon chiefly originates from g-C_3N_4 and GO, whereas oxygen mostly originates from $SnFe_2O_4$ and GO. While in CGS, the relative percentages of O, C, Fe, Sn, and N were found to be 46.8, 24.3, 15.2, 11.7, and 2.0%, respectively (Fig. 6b).

The high-resolution XPS spectrum of C 1s for CGS composite (Fig. 7a) shows three peaks at 284.1, 285.4, and 287.5 eV credited to sp^2 bonded carbon of g-C_3N_4 (C=C/N-C=N) and GO functionalities (C=O) (Yadav et al. 2019). The deconvoluted spectrum of N 1s attained with three various peaks situated at 401.3, 402.1, and 403.2 eV which belong to sp^2 bonded nitrogen (C-N=C), N-$(C)_3$, and N-H bonding units, respectively (Fig. 7b) (Chen et al. 2019). O 1s spectrum suited into two peaks, relating to Fe-O bond (530.7 eV) and -OH group (532.9 eV) of GO in CGS composite (Fig. 7c) (Shen et al. 2017). Sn 3d deconvoluted spectrum of CGS shows two peaks at 485.3 and 494.2 eV which can be assigned to Sn $3d_{5/2}$ and Sn $3d_{3/2}$, implying that Sn exists primarily as Sn^{2+}, presented in (Fig. 7d) (Luo et al. 2012). The two other peaks at 486.9 eV and 495.1 eV resulted from Sn^{4+} oxidation state (Liang et al. 2018). Hence, XPS results verify that both Sn^{4+} and Sn^{2+} ions occur in CGS composite. Fe 2p spectrum displays that the peaks at 710.1 and 723.3 eV with a spin–orbit splitting of 13.2 eV are designated to Fe $2p_{3/2}$ and Fe $2p_{1/2}$ (Fig. 7e). The strong satellite peak indicates the Fe^{3+} valence state in CGS composite (Wang et al. 2013). The above analysis shows the effective fabrication of a novel CGS composite.

Fig. 6 XPS analysis of GS, CS, and CGS composites. **a** Survey scans and **b** atomic percentages
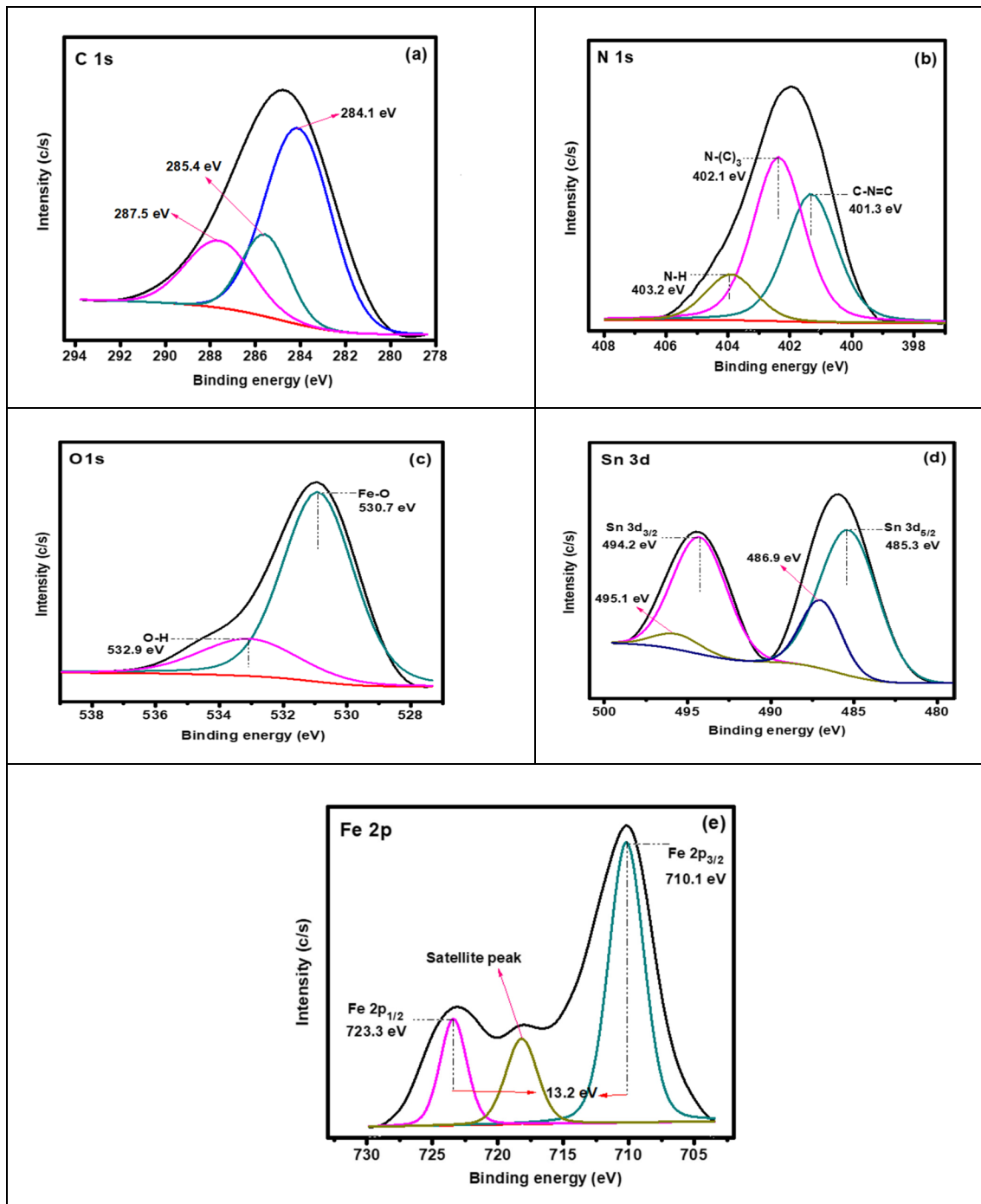
Fig. 7 High-resolution XPS spectra of **a** C 1s, **b** N 1s, **c** O 1s, **d** Sn 3d, and **e** Fe 2p spectra of ternary CGS composite

Optical analysis

By examining UV-Visible absorption spectra and figuring out band gap energies of binary GS, CS, and novel CGS nanocomposites in the 200–800-nm region, the optical response was evaluated. As illustrated in Fig. 8 using a Tauc plot, absorption edge of ternary CGS composite was located in a visible zone. Equation (3) was employed to evaluate the band gap energies of catalysts.

$$(ah\nu)^2 = B(h\nu - \mathrm{Eg}) \tag{3}$$

wherein $\mathrm{Eg} = h\nu$ when $\alpha h\nu = 0$. While energy (eV) is plotted versus $(\alpha h\nu)^2$. As illustrated in Fig. 8, calculating absorption

Fig. 8 Band gap energy estimation of binary CS, GS, and ternary CGS nanocomposites utilizing Tauc plot approach, and inset displays absorption spectra of nanocomposites
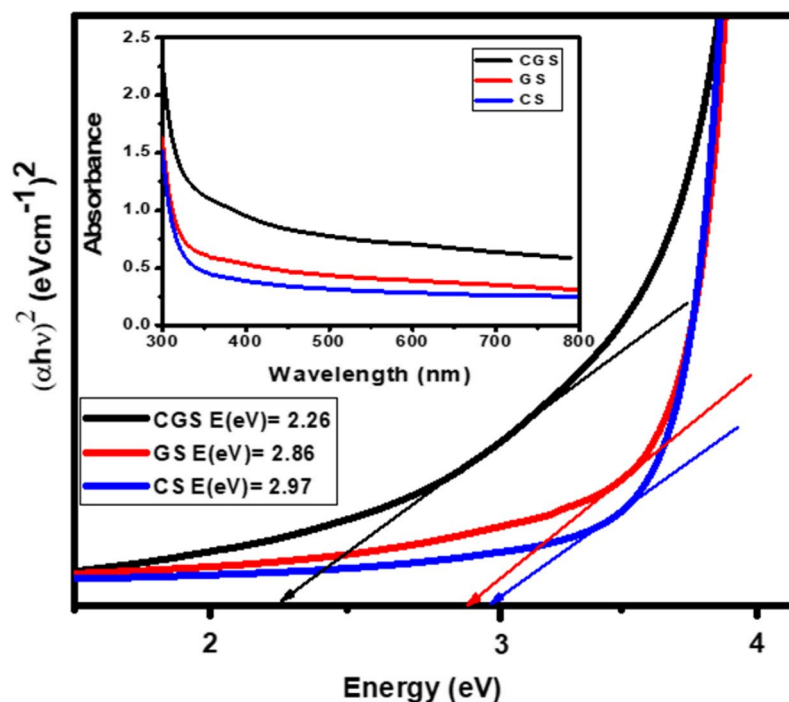
energy at the $h\nu$ value leads to an extrapolation of $\alpha = 0$. It was revealed that the calculated band gap energies were 2.26, 2.86, and 2.97 eV for CGS, GS, and CS composites. The absorption coefficient, proportionality constant, and light frequency are denoted here by the symbols, α, B, and ν. All photocatalysts exhibit strong absorption in the visible light spectrum, according to optical analysis.

Influence of degradation parameters

Effect of pH

Solution pH is a vital parameter in photo-Fenton-like reactions for the photodegradation of dyes (Bazarqan-Lari et al. 2011). It acts as an important part in the reaction mechanisms, containing an attack of $^{\bullet}$OH radical, oxidation through holes, and instant reduction by CB electrons (Alkaim et al. 2014). Also, the catalyst surface charge alters with varying pH values (Singh et al. 2020). The photodegradation of MB in a wide pH range (2–9) has been studied, illustrated in Fig. 9a. The highest photodegradation of MB using CGS, CS, and GS composites was attained at pH 5 and 4. In MB photodegradation, solution pH influenced the surface characteristics of photocatalysts. It was noticed that with a specific pH of dye solution, more degradation was observed. Using CGS composite the degradation efficacy of MB was 98% at pH 5 in 1 h. Increasing the pH of a solution results in a decrease in degradation efficacy.

This consequence could be because of the generation of Fenton's reagent at low pH to yield $^{\bullet}$OH radicals, which is the chief effective ROS for photodegradation of dyes (Sharma et al. 2015). The estimated pHpzc of CGS, GS, and CS was 4.76, 3.17, and 3.62. The pHpzc of binary CS, GS, and ternary CGS composite is depicted in Fig. S6. This outcome makes up a good agreement as the CGS composite shows best activity at pH higher than pHpzc of the photocatalyst. The pH higher than pHpzc surface of composite turn negatively charged which attracts MB (cationic dye) adsorption; consequently, better adsorption with improved photodegradation was attained (Nadeem et al. 2022). Therefore, pH 5 was used for further experiments using the CGS composite. While the binary CS and GS composite showed 85% and 87% degradation at pH 4 in sunlight with optimized conditions.

Effect of catalyst amount

The photocatalyst amount employed in an application is a significant factor related to both the photoactivity and the economic cost (Azizli et al. 2023a). For understanding the relationship between composite dosage and degradation efficacy, photodegradation of 10 ppm MB solution was examined within the range of 10–100 mg/100 mL, while maintaining all other variables fixed (pH = 5) for CGS and 4 for binary GS and CS, photocatalyst dosage= optimal for each photocatalyst, and contact time of 60 min. Figure 9b depicts the effect of the catalyst amount using CGS, GS, and CS on the photocatalytic removal of MB. The results
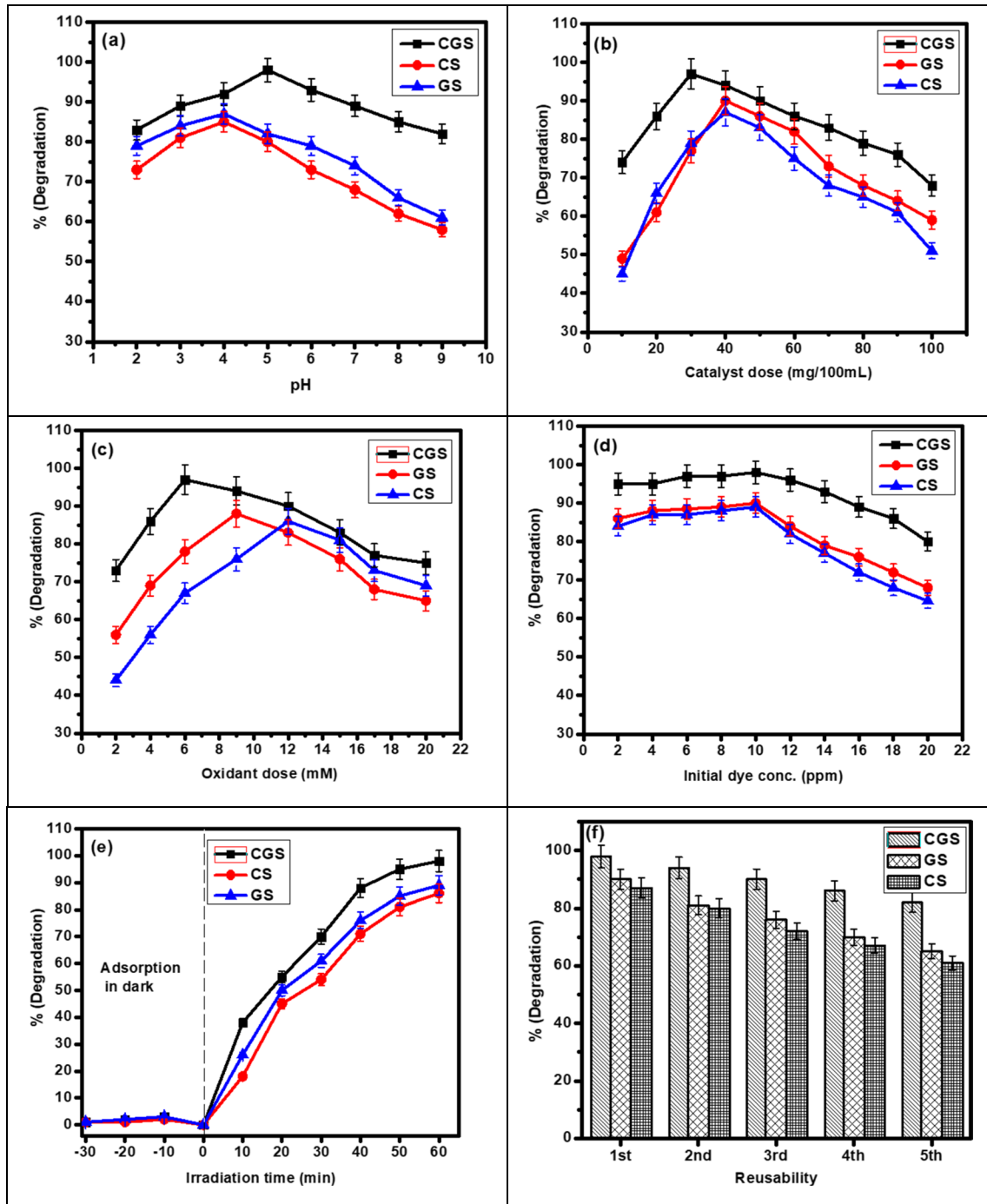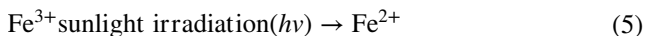
Fig. 9 Factors affecting the MB dye photodegradation rate of nanocomposites **a** pH, **b** composite amount, **c** oxidant dosage,) initial dye concentration, **e** time, and **f** reusability

indicate that degradation of MB was meaningfully affected by photocatalyst dosage. The photodegradation efficacy of CGS was enhanced from 77 to 98% as the composite dosage was enhanced from 10 to 30 mg. This is because additional active spots were accessible for catalytic breakdown of H_2O_2 at a faster rate to produce additional hydroxyl radicals (Guo et al. 2014). However, degradation efficiency slightly

declined from 98 to 90% when composite dose was raised to 50 mg, and drastically decreased beyond 50 mg. This might be attributed to hindrance influence brought about by more Fe ions in heterogeneous photo-Fenton approach that serves as scavengers as displayed in Eq. (4) (Nadeem et al. 2021). Furthermore, a higher catalyst dose would enhance reaction turbidity and decrease sunlight radiation intensity necessary

for photoreduction of Fe^{3+} in Eq. (5) (Guo et al. 2014). Further, the Fe^{2+} will combine with OH^- and produce $Fe(OH)_2$ (sludge) as shown in Eq. (6) (Bazargan-Lari et al. 2014).

$$Fe^{2+} + \cdot OH \rightarrow Fe^{3+} + OH^- \qquad (4)$$

$$Fe^{3+} \text{ sunlight irradiation}(h\nu) \rightarrow Fe^{2+} \qquad (5)$$

$$Fe^{2+} + 2OH^- \rightarrow Fe(OH)_2 \qquad (6)$$

Both binary CS and GS nanocomposites exhibited improved degradation at an ideal composite dosage of 40 mg/100 mL as presented in Fig. 9b. Therefore, composite dosage determines the photocatalyst limit for specific organic contaminants in wastewater beyond which photodegradation efficiency ultimately declines.

Effect of H_2O_2 dose

The oxidant dosage is a significant parameter for organic contaminant photodegradation in heterogeneous photo-Fenton method (Guo et al. 2015). The convenient way to improve the degradation of dyes is to introduce a robust oxidant into the reaction system (Mohammadzadeh et al. 2020). H_2O_2 enhances the generation rate of $\cdot OH$ radicals and improves organic pollutant degradation at lower concentrations. This is because of the effective production of $\cdot OH$ radicals and prevents the e^-/h^+ pair recombination since H_2O_2 is an electron acceptor (Reza et al. 2017; Zhang et al. 2018). H_2O_2 is deemed as an utmost strong oxidizing agent and yields 2 mol of $\cdot OH$ ($H_2O_2 + h\nu = 2 \cdot OH$), accompanied by contact with dye molecules (Khan et al. 2022b). H_2O_2 is a widely used oxidant because of its lower cost, higher activity, stability, and environment friendliness as it produces H_2O as a by-product (Tahir et al. 2021).

The optimization process of H_2O_2 was carried out by following experimental conditions such as pH = 5 for CGS and 4 for CS and GS, catalyst dosage = 30 mg for CGS and 40 mg/100 mL for CS and GS, 10 ppm MB dye concentration, and 60 min irradiation time. As illustrated in Fig. 9c, the influence of H_2O_2 dose on MB photodegradation was observed by varying concentrations of H_2O_2 from 2 to 20 mM.

Once H_2O_2 dosage was raised from 2 to 6 mM, MB elimination efficiency improved accordingly from 71 to 98% using CGS composite. Increasing the concentration of H_2O_2 in MB dye solution resulted in an enhancement in the formation of $\cdot OH$ radicals (Naseem et al. 2016). Further, increasing the concentration of H_2O_2 above 6 mM could not increase the MB degradation. This is because H_2O_2 at higher concentrations behaves as a scavenger of extremely strong $\cdot OH$ radicals leading to production of lesser reactive species for instance $\cdot OOH$ as shown in Eq. (7) (Wang et al. 2020).

Hydroperoxyl radicals showed much lesser oxidation abilities and could not participate in the photodegradation of MB Eq. (8), which led to a decline in degradation efficacy (Rache et al. 2014). Such types of reactions decreased possibility of attacking MB molecules by $\cdot OH$ radicals and resulted in declining the photodegradation efficiency (Herney-Ramirez et al. 2010). Consequently, a further increase in H_2O_2 concentration above its optimal level would drop the photodegradation efficacy.

$$H_2O_2 + \cdot OH \rightarrow \cdot OOH + H_2O \qquad (7)$$

$$\cdot OOH + \cdot OH \rightarrow H_2O + O_2 \qquad (8)$$

Both binary GS and CS nanocomposites displayed improved degradation at an optimum oxidant dosage of 9 and 12 mM as shown in Fig. 9c. Hence, an optimal dosage of H_2O_2 is critical for attaining superior photocatalytic activity.

Effect of IDC

Dye degradation efficiency relies on its nature, concentration, and existence of other molecules in a solution (Salama et al. 2018). The degradation efficacy of MB was observed by altering MB dye dose from 2 to 20 ppm for CGS, CS, and GS composites maintaining all other experimental conditions constant (Fig. 9d). The degradation rate enhanced quickly at initial MB concentrations, respectively. The photodegradation rate improved with increasing MB dye concentration from 2 to 10 ppm owing to the availability of additional active spots on photocatalyst surface (Alkaykh et al. 2020). However, a negative impact on the degradation rate was noticed for the increase in MB dose above 10 ppm. This influence might be because of additional MB dye molecules, which might be adsorbed on the surface of photocatalyst and occupy photocatalyst active spots once the dose of dye was increased (Ahmed et al. 2016). This led to lesser $\cdot OH$ radicals at the photocatalyst surface (Rache et al. 2014). Hence, a reaction between photocatalyst and H_2O_2 was repressed, which reduced the degradation rate of MB (Bazargan-Lari et al. 2011). Consequently, this required additional photocatalyst and a prolonged time of reaction for increased MB dye concentration.

Effect of contact time

Contact time and adsorption equilibrium between photocatalyst and dye is an essential parameter that determines the degradation (Ashrafi et al. 2020). Figure 9e shows the impact of illumination time on MB elimination by CS, GS, and ternary CGS. The results indicate that rate of dye elimination is linked directly to contact time, which implies that photodegradation improves with increasing irradiation time

(Prasert et al. 2020). Due to the greater contact time, an enhanced rate of reaction takes place leading to enhanced photogeneration of e^-/h^+ pair. Ultimately, this enhances probability of contact between MB molecule and e^-/h^+ pairs (Ebrahimi et al. 2021). The photoactivity of photocatalysts increases with prolonged contact time, as contaminant molecules are exposed to more free radicals for a longer period, which increases the photodegradation rate (Pooladi and Bazargan-Lari 2020).

Reusability

From the economic and environmental point of view, it is necessary to investigate the stability and reusability of a photocatalyst (Azizli et al. 2023b). Afterwards, the degradation reaction was completed, and composites were restored using the magnet washed three times with distilled water and oven dried at 60 °C and used again for a later cycle. At the same optimized conditions, all reusability study is performed for each composite, i.e., pH 5, composite amount 30 mg/100 mL, oxidant dose 6 mM, IDC 10 ppm for CGS, and pH 4, IDC 10 ppm, composite dosage 40 mg/100 mL for GS, and CS composites. According to Fig. 9f, the photocatalyst can be utilized up to five times and maintain 84% photocatalytic activity with minimal product yield loss. The outcomes showed that CGS nanocomposite displays a higher degree of reusability and mechanical stability.

Kinetics of photodegradation reaction

For the photodegradation of MB dye, first and second kinetic models were studied by binary and ternary composites. In Eqs. (9) and (10), the expression for each model is represented.

$$\text{First} - \text{order} : \ln \frac{C_o}{C_t} = K_1 t \qquad (9)$$

$$\text{Second order} : \frac{1}{C_t} - \frac{1}{C_o} = K_2 t \qquad (10)$$

A linear relationship between reaction time and $\ln (C_o/C_t)$ is shown in Fig. 10, wherein C_o and C_t are initial concentrations, representing that degradation of MB by binary and ternary composites follow first order. When time is plotted versus C_o/C_t, a straight line is depicted, where the slope of which linear regression becomes equivalent to rate constant K of first order. A greater rate constant K of CGS for first order than binary composites specifies that CGS nanocomposite is highly efficient in solar light than binary composites. R^2 values for first-order for binary CS, GS, and novel CGS nanocomposites are 0.9773, 0.9831, and 0.9920,
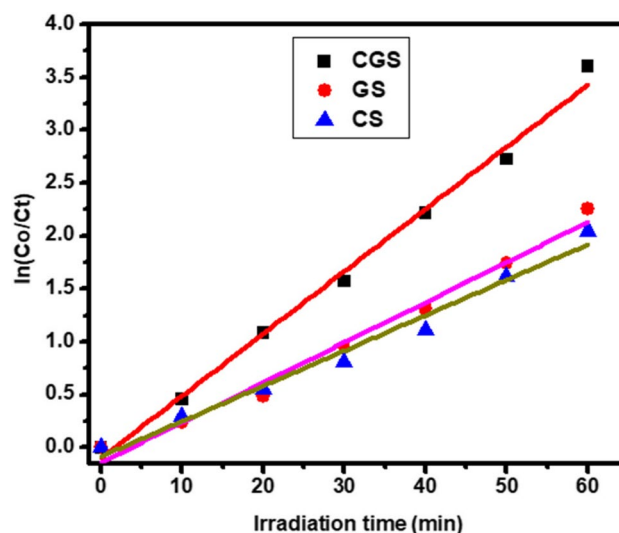

Fig. 10 First-kinetic model using binary and ternary composites

proposing that CGS composite follows first-kinetic model effectively. Values of R^2 for kinetic models are illustrated in Table 1.

Radical scavenging and proposed mechanism

The effects of scavenging agents on the dye degradation rate were studied to estimate possible ROS that is accountable for photodegradation process (Mushtaq et al. 2020). Several reactive species, for example, electron (e^-), hydroxyl radical ($^\bullet OH$), and holes (h^+), perform an essential part in the degradation of dyes (Khan et al. 2022a). Therefore, to examine the important species included in photocatalytic method, a radical scavenging study was carried out under sunlight irradiation. Ten millimolar of EDTA, $K_2Cr_2O_7$, and DMSO were employed to scavenge holes, electrons, and $^\bullet OH$ radicals. Figure 11 shows that DMSO is main scavenger for MB dye photodegradation using CGS composite, as DMSO addition; the degradation rate reduced from 98 to 38%. The EDTA reduced the photodegradation from 98 to 51% representing that holes have also an influencing part in degradation process. The addition of $K_2Cr_2O_7$ indicates that electrons play a little role in MB degradation by CGS.

The proposed photocatalytic mechanism for the CGS nanocomposite under sunlight irradiation is shown in Fig. 12. Under sunlight, both $SnFe_2O_4$ and $g\text{-}C_3N_4$ are excited, and photoinduced electrons from CB of $SnFe_2O_4$ move towards the $g\text{-}C_3N_4$ VB through GO as an electron mediator, causing segregation between VB holes of $SnFe_2O_4$ and CB electrons of $g\text{-}C_3N_4$. The photoinduced holes in VB of $SnFe_2O_4$ are captured through H_2O to form $^\bullet OH$ radicals.

Table 1 Kinetic model fitting of first and second order for MB degradation using composites

Composites	Optimized conditions				1st order		2nd order	
	pH	Catalyst dose (mg/100 mL)	H$_2$O$_2$ dosage (mM)	IDC (ppm)	R^2	K_1 (min^{-1})	R^2	K_2 (µL mol^{-1} min^{-1})
CGS	5	30 mg	6 mM	10 ppm	0.9920	0.05	0.6750	0.325
GS	4	40 mg	9 mM	10 ppm	0.9831	0.037	0.7074	0.061
CS	4	40 mg	12 mM	10 ppm	0.9773	0.033	0.7275	0.067
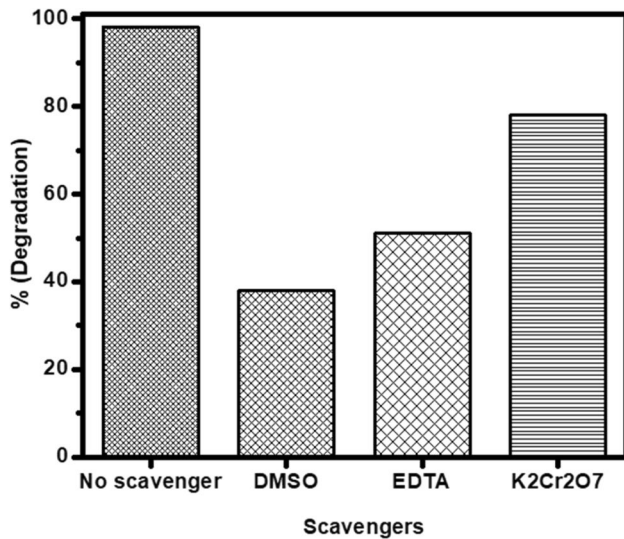
Fig. 11 Scavenging study of ternary CGS composite

Furthermore, photoinduced electrons in CB of g-C$_3$N$_4$ are captured via dissolved oxygen to produce $^\bullet$O$_2^-$ radical anion. Thus, $^\bullet$O$_2^-$ anion reacts with the H$_2$O$_2$ and forms the hydroxyl radical which effectively degrades the MB dye. After a series of reactions, MB eventually degrades into CO$_2$, H$_2$O, and specific inorganic ions. Hence, it proposes the CGS composite as a Z-scheme photocatalyst, which owns longer charge carrier lifetime, higher charge separation efficiency, and efficient photocatalytic activity. Specifically, GO can promote the movement of electrons from SnFe$_2$O$_4$ to g-C$_3$N$_4$ and repress reverse movement of electrons to SnFe$_2$O$_4$. Consequently, photoactivity of Z-scheme g-C$_3$N$_4$/SnFe$_2$O$_4$ nanocomposite was significantly improved afterwards incorporating the GO as a solid support electron facilitator. Table 2 shows a comparison table of previously reported SnFe$_2$O$_4$-based GO and g-C$_3$N$_4$ composites.
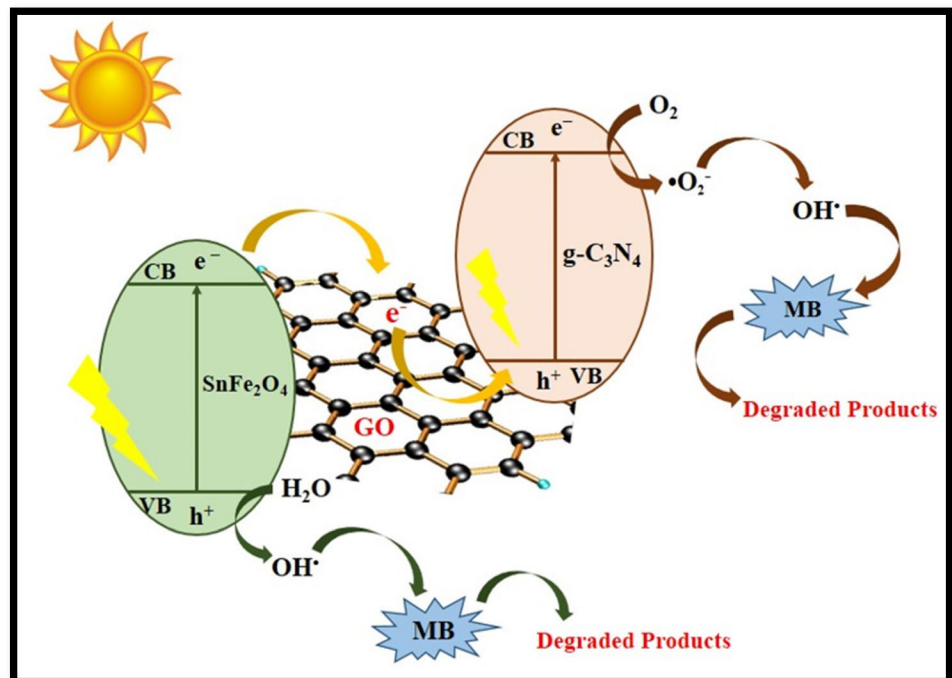
Fig. 12 The possible photodegradation mechanism of g-C$_3$N$_4$/GO/SnFe$_2$O$_4$ (CGS) composite

Table 2 Comparison table of $SnFe_2O_4$-based GO and $g\text{-}C_3N_4$ composites

Sr. No.	Photocatalyst	Preparation approach	Light source	Contact time (min)	H_2O_2 conc. (mM)	Model pollutant/degradation (%)	Other applications	References
1.	$SnFe_2O_4/g\text{-}C_3N_4$	Solvothermal method	-	-	-	-	Photocatalytic CO_2 reduction	(Jia et al. 2020)
2.	$g\text{-}C_3N_4/SnFe_2O_4$	Solvothermal method	Visible light irradiation	300 min	-	Chlorotetracycline (67%)	-	(Jia et al. 2017)
3.	$SnFe_2O_4$–graphene hybrid films	Electrophoretic deposition (EPD)	-	-	-	-	Anode for lithium-ion batteries	(Xu et al. 2017)
4.	Sulfur-doped $SnFe_2O_4$/graphene nanohybrids	Facile solvothermal method	Visible light irradiation	240 min	-	Chlorotetracycline (70%)	-	(Jia et al. 2017)
5.	$SnFe_2O_4/g\text{-}C_3N_4$ hybrid photocatalyst	Facile in-situ precipitation method	Visible-light illumination	-	-	Rh B, MO, MB	Hydrogen production	(Jo et al. 2020)
6.	$g\text{-}C_3N_4/SnFe_2O_4$	Solvothermal method	Sunlight irradiation	60 min	12 mM	MB (85%)	-	This work
7.	$GO/SnFe_2O_4$	Solvothermal method	Sunlight irradiation	60 min	9 mM	MB (87%)	-	This work
8.	$g\text{-}C_3N_4/GO/SnFe_2O_4$	Solvothermal method	Sunlight irradiation	60 min	6 mM	MB (98%)	-	This work

Conclusion

In this work, for the first time, $g\text{-}C_3N_4$ heterojunction with $SnFe_2O_4$ and GO as a supported electron mediator is reported. Ternary CGS composite was observed as an efficient photocatalyst for environmental remediation in solar light irradiation. CGS composite was fabricated successfully using an in situ solvothermal approach and was well-characterized through numerous analyses, for instance, SEM-EDX, XRD, FTIR, UV-vis spectroscopy, TEM, and XPS. CGS composite was examined for photodegradation of methylene blue in sunlight. Compared with binary CS and GS composites, novel CGS composite exhibited 98% improved photodegradation of MB in 1 h at ideal conditions such as pH (5), composite dosage (30 mg/100 mL), dye concentration (10 ppm), and H_2O_2 dosage (6 mM). Furthermore, the appealing features of CGS, for example, are easy synthesis, outstanding photocatalytic performance, magnetically separable and outstanding durability. Z-scheme ternary CGS composite achieved in the present study offers a new perceptive to improve the recyclability and photoefficiency of $g\text{-}C_3N_4$-based photocatalyst.

Declarations

Ethical approval and consent to participate Not applicable.

Consent for publication All the authors agree to publish this article.

Competing interests The authors declare no competing interests.

References

Ahmad MA, Aslam S, Mustafa F, Arshad U (2021) Synergistic antibacterial activity of surfactant free Ag–GO nanocomposites. Sci Rep 11:196–205

Ahmed Y, Yaakob Z, Akhtar P (2016) Degradation and mineralization of methylene blue using a heterogeneous photo-Fenton catalyst under visible and solar light irradiation. Catal Sci Technol 6:1222–1232

Akhundi A, Habibi-Yangjeh A (2016) Ternary magnetic $g\text{-}C_3N_4/Fe_3O_4/AgI$ nanocomposites: novel recyclable photocatalysts with enhanced activity in degradation of different pollutants under visible light. Mater Chem Phys 174:59–69

Alkaim A, Aljeboree A, Alrazaq N, Baqir S, Hussein F, Lilo A (2014) Effect of pH on adsorption and photocatalytic degradation efficiency of different catalysts on removal of methylene blue. Chem Asian J 26:8445–8448

Alkaykh S, Mbarek A, Ali-Shattle EE (2020) Photocatalytic degradation of methylene blue dye in aqueous solution by $MnTiO_3$ nanoparticles under sunlight irradiation. Heliyon 6:03663–03669

Ashrafi H, Akhond M, Absalan G (2020) Adsorption and photocatalytic degradation of aqueous methylene blue using nanoporous carbon nitride. J Photochem Photobiol A: Chem 396:112533–112544

Azizli MJ, Ghadami A, Vafa E, Rezaeeparto K, Parham S, Mokhtary M, Jahankhah Z, Azizli F, Bazargan-Lari R, Amani AM (2023) Compatibilization of immiscible PA6/PLA nanocomposites using graphene oxide and PTW compatibilizer for high thermal and mechanical applications. J Polym Environ 11:1–17

Azizli MJ, Vafa E, Rezaeeparto K, Parham S, Mokhtary M, Jahankhah Z (2023) Preparation, characterization, and compatibilization of novel rubber nanocomposites for mechanical applications: relationship between electrical properties, morphology, and rheology. J Adhes Sci Technol 11:1–25

Bambaeero A, Bazargan-Lari R (2021) Simultaneous removal of copper and zinc ions by low cost natural snail shell/hydroxyapatite/chitosan composite. Chin J Chem Eng 33:221–230

Bazargan-Lari R, Bahrololoom M, Nemati A (2011) Sorption behavior of Zn (II) ions by low cost and biological natural hydroxyapatite/chitosan composite from industrial waste water. J Food Agric Environ 9:892–897

Bazargan-Lari R, Zafarani HR, Bahrololoom ME, Nemati A (2014) Removal of Cu (II) ions from aqueous solutions by low-cost natural hydroxyapatite/chitosan composite: equilibrium, kinetic and thermodynamic studies. J Taiwan Inst Chem Eng 45:1642–1648

Bazarqan-Lari R, Bahrololoom M, Nemati A (2011) Adsorption of Cu (II) ions from industrial wastewater on natural hydroxyapatite extracted from bone ash. J Food Agric Environ 2:652–657

Bindu K, Sridharan K, Ajith K, Lim H, Nagaraja H (2016) Microwave assisted growth of stannous ferrite microcubes as electrodes for potentiometric nonenzymatic H_2O_2 sensor and supercapacitor applications. Electrochim Acta 217:139–149

Borthakur S, Saikia L (2019) $ZnFe_2O_4$@ g-C_3N_4 nanocomposites: an efficient catalyst for Fenton-like photodegradation of environmentally pollutant Rhodamine B. J Environ Chem Eng 7:103035–103045

Cai C, Zhang Z, Liu J, Shan N, Zhang H, Dionysiou DD (2016) Visible light-assisted heterogeneous Fenton with $ZnFe_2O_4$ for the degradation of Orange II in water. Appl Catal B 182:456–468

Chen L, Ma W, Dai J, Zhao J, Li C, Yan Y (2016) Facile synthesis of highly efficient graphitic-C_3N_4/$ZnFe_2O_4$ heterostructures enhanced visible-light photocatalysis for spiramycin degradation. J Photochem Photobiol A: Chem 328:24–32

Chen Z, Chen P, Xing P, Hu X, Lin H, Zhao L, Wu Y, He Y (2019) Rapid fabrication of $KTa_{0.75}Nb_{0.25}$/g-C_3N_4 composite via microwave heating for efficient photocatalytic H_2 evolution. Fuel 241:1–11

Deng Y, Tang L, Zeng G, Zhu Z, Yan M, Zhou Y, Wang J, Liu Y, Wang J (2017) Insight into highly efficient simultaneous photocatalytic removal of Cr (VI) and 2, 4-diclorophenol under visible light irradiation by phosphorus doped porous ultrathin g-C_3N_4 nanosheets from aqueous media: performance and reaction mechanism. Appl Catal B 203:343–354

Ebrahimi A, Jafari N, Ebrahimpour K, Karimi M, Rostamnia S, Behnami A, Ghanbari R, Mohammadi A, Rahimi B, Abdolahnejad A (2021) A novel ternary heterogeneous TiO_2/$BiVO_4$/NaY-Zeolite nanocomposite for photocatalytic degradation of microcystin-leucine arginine (MC-LR) under visible light. Ecotoxicol Environ Saf 210:111862–111874

Fu Y, Xiong P, Chen H, Sun X, Wang X (2012) High photocatalytic activity of magnetically separable manganese ferrite–graphene heteroarchitectures. Ind Eng Chem 51:725–731

Fu J, Yu J, Jiang C, Cheng B (2018) g-C_3N_4-based heterostructured photocatalysts. Adv Energy Mater 8:1701503–1701534

Fu J, Xu Q, Low J, Jiang C, Yu J (2019) Ultrathin 2D/2D WO_3/g-C_3N_4 step-scheme H_2-production photocatalyst. Appl Catal B: Environ 243:556–565

Gebreslassie G, Bharali P, Chandra U, Sergawie A, Boruah PK, Das MR, Alemayehu E (2019) Novel g-C_3N_4/graphene/$NiFe_2O_4$ nanocomposites as magnetically separable visible light driven photocatalysts. J Photochem Photobiol A: Chem 382:111960–111970

Guo S, Zhang G, Wang J (2014) Photo-Fenton degradation of rhodamine B using Fe_2O_3–Kaolin as heterogeneous catalyst: characterization, process optimization and mechanism. J Colloid Interface Sci 433:1–8

Guo S, Zhang G, Jimmy CY (2015) Enhanced photo-Fenton degradation of rhodamine B using graphene oxide–amorphous $FePO_4$ as effective and stable heterogeneous catalyst. J Colloid Interface Sci 448:460–466

Guo F, Shi W, Li M, Shi Y, Wen H (2019) 2D/2D Z-scheme heterojunction of $CuInS_2$/g-C_3N_4 for enhanced visible-light-driven photocatalytic activity towards the degradation of tetracycline. Sep Purif Technol 210:608–615

He R, Zhou J, Fu H, Zhang S, Jiang C (2018) Room-temperature in situ fabrication of Bi_2O_3/g-C_3N_4 direct Z-scheme photocatalyst with enhanced photocatalytic activity. Appl Surf Sci 430:273–282

Herney-Ramirez J, Vicente MA, Madeira LM (2010) Heterogeneous photo-Fenton oxidation with pillared clay-based catalysts for wastewater treatment: a review. Appl Catal B 98:10–26

Hu X, Wang H, Liu Y (2016) Statistical analysis of main and interaction effects on Cu (II) and Cr (VI) decontamination by nitrogen–doped magnetic graphene oxide. Sci Rep 6:1–11

Hu X, Wang W, Xie G, Wang H, Tan X, Jin Q, Zhou D, Zhao Y (2019) Ternary assembly of g-C_3N_4/graphene oxide sheets/$BiFeO_3$ heterojunction with enhanced photoreduction of Cr (VI) under visible-light irradiation. Chemosphere 216:733–741

Jia Y, Wu C, Lee B, Liu C, Kang S, Lee T, Park YC, Yoo R, Lee W (2017) Magnetically separable sulfur-doped $SnFe_2O_4$/graphene nanohybrids for effective photocatalytic purification of wastewater under visible light. J Hazard Mater 338:447–457

Jia Y, Ma H, Zhang W, Zhu G, Yang W, Son N, Kang M, Liu C (2020) Z-scheme $SnFe_2O_4$-graphitic carbon nitride: reusable, magnetic catalysts for enhanced photocatalytic CO_2 reduction. Chem Eng J 383:123172–123183

Jo W-K, Moru S, Tonda S (2020) Magnetically responsive $SnFe_2O_4$/g-C_3N_4 hybrid photocatalysts with remarkable visible-light-induced performance for degradation of environmentally hazardous substances and sustainable hydrogen production. Appl Surf Sci 506:144939–144950

Khan F, Zahid M, Bhatti H, Jamil Y (2022) Degradation of persistent organic pollutant using Ag-doped ZnO-ZnS–polyaniline composite as photocatalyst. Int J Environ Sci Technol 5:1–16

Khan I, Saeed K, Zekker I, Zhang B, Hendi AH, Ahmad A, Ahmad S, Zada N, Ahmad H, Shah LA (2022) Review on methylene blue: its properties, uses, toxicity and photodegradation. Water 14:242–272

Kong HJ, Won DH, Kim J, Woo SI (2016) Sulfur-doped g-C_3N_4/$BiVO_4$ composite photocatalyst for water oxidation under visible light. Chem Mater 28:1318–1324

Lee K-T, Lu S-Y (2015) A cost-effective, stable, magnetically recyclable photocatalyst of ultra-high organic pollutant degradation efficiency: $SnFe_2O_4$ nanocrystals from a carrier solvent assisted interfacial reaction process. J Mater Chem A 3:12259–12267

Liang C, Kim B, Yang S, Liu Y, Woellner CF, Li Z, Vajtai R, Yang W, Wu J, Kenis PJ (2018) High efficiency electrochemical reduction of CO_2 beyond the two-electron transfer pathway on grain boundary rich ultra-small SnO_2 nanoparticles. J Mater Chem 6:10313–10319

Liu W, Shen J, Yang X, Liu Q, Tang H (2018) Dual Z-scheme g-C_3N_4/Ag_3PO_4/Ag_2MoO_4 ternary composite photocatalyst for solar oxygen evolution from water splitting. Appl Surf Sci 456:369–378

Lu N, Wang P, Su Y, Yu H, Liu N, Quan X (2019) Construction of Z-scheme g-C$_3$N$_4$/RGO/WO$_3$ with in situ photoreduced graphene oxide as electron mediator for efficient photocatalytic degradation of ciprofloxacin. Chemosphere 215:444–453

Luo H, Liang LY, Cao HT, Liu ZM, Zhuge F (2012) Structural, chemical, optical, and electrical evolution of SnOx films deposited by reactive rf magnetron sputtering. ACS Appl Mater Interfaces 4:5673–5677

Ma H, Zhuo Q, Wang B (2009) Electro-catalytic degradation of methylene blue wastewater assisted by Fe$_2$O$_3$-modified kaolin. Chem Eng J 155:248–253

Martínez-Huitle CA, Brillas E (2009) Decontamination of wastewaters containing synthetic organic dyes by electrochemical methods: a general review. Appl Catal B 87:105–145

Miklos DB, Remy C, Jekel M, Linden KG, Drewes JE, Hübner U (2018) Evaluation of advanced oxidation processes for water and wastewater treatment–a critical review. Water Res 139:118–131

Mohammadzadeh A, Khoshghadam-Pireyousefan M, Shokrianfard-Ravasjan B, Azadbeh M, Rashedi H, Dibazar M, Mostafaei A (2020) Synergetic photocatalytic effect of high purity ZnO pod shaped nanostructures with H$_2$O$_2$ on methylene blue dye degradation. J Alloys Compd 845:156333–156344

Mushtaq F, Zahid M, Mansha A, Bhatti I, Mustafa G, Nasir S, Yaseen M (2020) MnFe$_2$O$_4$/coal fly ash nanocomposite: a novel sunlight-active magnetic photocatalyst for dye degradation. Int J Environ Sci Technol 17:4233–4248

Nadeem N, Abbas Q, Yaseen M, Jilani A, Zahid M, Iqbal J, Murtaza A, Janczarek M, Jesionowski T (2021) Coal fly ash-based copper ferrite nanocomposites as potential heterogeneous photocatalysts for wastewater remediation. Appl Surf Sci 565:150542–150555

Nadeem N, Yaseen M, Rehan ZA, Zahid M, Shakoor RA, Jilani A, Iqbal J, Rasul S, Shahid I (2022) Coal fly ash supported CoFe$_2$O$_4$ nanocomposites: synergetic Fenton-like and photocatalytic degradation of methylene blue. Environ Res 206:112280–112293

Naseem Z, Bhatti HN, Sadaf S, Noreen S, Ilyas S (2016) Sorption of uranium (VI) by Trapa bispinosa from aqueous solution: effect of pretreatments and modeling studies. Desalin Water Treat 57:11121–11132

Ossonon BD, Bélanger D (2017) Synthesis and characterization of sulfophenyl-functionalized reduced graphene oxide sheets. RSC adv 7:27224–27234

Paulchamy B, Arthi G, Lignesh B (2015) A simple approach to stepwise synthesis of graphene oxide nanomaterial. J Nanomed Nanotechnol 6:1–4

Pooladi A, Bazargan-Lari R (2020) Simultaneous removal of copper and zinc ions by chitosan/hydroxyapatite/nano-magnetite composite. J Mater Res Technol 9:14841–14852

Pooladi A, Bazargan-Lari R (2023) Adsorption of zinc and copper ions simultaneously on a low-cost natural chitosan/hydroxyapatite/snail shell/nano-magnetite composite. Cellulose 30:5687–5705

Prasert A, Sontikaew S, Sriprapai D, Chuangchote S (2020) Polypropylene/ZnO nanocomposites: mechanical properties, photocatalytic dye degradation, and antibacterial property. Materials 13:914–930

Rache ML, García AR, Zea HR, Silva AM, Madeira LM, Ramírez JH (2014) Azo-dye orange II degradation by the heterogeneous Fenton-like process using a zeolite Y-Fe catalyst—kinetics with a model based on the Fermi's equation. Appl Catal B 146:192–200

Rai P, Gautam RK, Banerjee S, Rawat V, Chattopadhyaya M (2015) Synthesis and characterization of a novel SnFe$_2$O$_4$@activated carbon magnetic nanocomposite and its effectiveness in the removal of crystal violet from aqueous solution. J Environ Chem Eng 3:2281–2291

Ren J, Wu Y, Zou H, Dai Y, Sha D, Chen M, Wang J, Pan J, Yan X (2016) Synthesis of a novel CeVO$_4$/graphitic C$_3$N$_4$ composite with enhanced visible-light photocatalytic property. Mater Lett 183:219–222

Reza KM, Kurny A, Gulshan F (2017) Parameters affecting the photocatalytic degradation of dyes using TiO$_2$: a review. Appl Water Sci 7:1569–1578

Saher R, Hanif M, Mansha A, Javed H, Zahid M, Nadeem N, Mustafa G, Shaheen A, Riaz O (2021) Sunlight-driven photocatalytic degradation of rhodamine B dye by Ag/FeWO$_4$/g-C$_3$N$_4$ composites. Int J Environ Sci Technol 18:927–938

Salama A, Mohamed A, Aboamera NM, Osman T, Khattab A (2018) Photocatalytic degradation of organic dyes using composite nanofibers under UV irradiation. Appl Nanosci 8:155–161

Schwinghammer K, Mesch MB, Duppel V, Ziegler C, Senker JR, Lotsch BV (2014) Crystalline carbon nitride nanosheets for improved visible-light hydrogen evolution. J Am Chem Soc 136:1730-1733

Sharma R, Bansal S, Singhal S (2015) Tailoring the photo-Fenton activity of spinel ferrites (MFe$_2$O$_4$) by incorporating different cations (M= Cu, Zn, Ni and Co) in the structure. RSC Adv 5:6006–6018

Shen L, Xing Z, Zou J, Li Z, Wu X, Zhang Y, Zhu Q, Yang S, Zhou W (2017) Black TiO$_2$ nanobelts/g-C$_3$N$_4$ nanosheets laminated heterojunctions with efficient visible-light-driven photocatalytic performance. Sci Rep 7:41978–41988

Singh R, Ladol J, Khajuria H, Sheikh HN (2017) Nitrogen doped graphene nickel ferrite magnetic photocatalyst for the visible light degradation of methylene blue. Acta Chim Slov 64:170–178

Singh RK, Behera SS, Singh KR, Mishra S, Panigrahi B, Sahoo TR, Parhi PK, Mandal D (2020) Biosynthesized gold nanoparticles as photocatalysts for selective degradation of cationic dye and their antimicrobial activity. J Photochem Photobiol A: Chem 400:112704–112713

Solís M, Solís A, Pérez HI, Manjarrez N, Flores M (2012) Microbial decolouration of azo dyes: a review. Process Biochem 47:1723–1748

Sudhaik A, Raizada P, Shandilya P, Jeong D-Y, Lim J-H, Singh P (2018) Review on fabrication of graphitic carbon nitride based efficient nanocomposites for photodegradation of aqueous phase organic pollutants. J Ind Eng Chem 67:28–51

Tabasum A, Zahid M, Bhatti HN, Asghar M (2018) Fe$_3$O$_4$-GO composite as efficient heterogeneous photo-Fenton's catalyst to degrade pesticides. Mater Res Express 6:015608–015630

Tahir S, Qazi UY, Naseem Z, Tahir N, Zahid M, Javaid R, Shahid I (2021) Deep eutectic solvents as alternative green solvents for the efficient desulfurization of liquid fuel: a comprehensive review. Fuel 305:121502–121518

Tahir S, Tahir N, Hussain T, Naseem Z, Zahid M, Mustafa G (2022) Non-photocatalytic and photocatalytic inactivation of viruses using antiviral assays and antiviral nanomaterials. In: Thangadurai D, Islam S, Oluwaseun AC (Eds.). Viral and antiviral nanomaterials, 1st edn. CRC Press, Boca Raton, pp 139–164

Wacławek S, Lutze HV, Grübel K, Padil VV, Černík M, Dionysiou DD (2017) Chemistry of persulfates in water and wastewater treatment: a review. Chem Eng J 330:44–62

Wan W, Yu S, Dong F, Zhang Q, Zhou Y (2016) Efficient C$_3$N$_4$/graphene oxide macroscopic aerogel visible-light photocatalyst. J Mater Chem 4:7823–7829

Wang M, Sun L, Cai J, Huang P, Su Y, Lin C (2013) A facile hydrothermal deposition of ZnFe$_2$O$_4$ nanoparticles on TiO$_2$ nanotube arrays for enhanced visible light photocatalytic activity. J Mater Chem 1:12082–12087

Wang Q, Wang X, Liu S, Li R (2020) Efficient decolorization of methylene blue catalyzed by MgFe-layered double hydroxides in the presence of hydrogen peroxide. Water Sci Technol 81:781–789

Wu D, Li J, Guan J, Liu C, Zhao X, Zhu Z, Ma C, Huo P, Li C, Yan Y (2018) Improved photoelectric performance via fabricated

heterojunction g-C$_3$N$_4$/TiO$_2$/HNTs loaded photocatalysts for photodegradation of ciprofloxacin. J Ind Eng Chem 64:206–218

Xu T, Meng Q, Yang M, Zhi W, Cao B (2017) Electrophoretic deposition of SnFe$_2$O$_4$–graphene hybrid films as anodes for lithium ion batteries. Aust J Chem 70:1073–1081

Yadav RS, Kuřitka I, Vilčáková J, Machovský M, Škoda D, Urbánek P, Masař M, Gořalik M, Urbánek M, Kalina L (2019) Polypropylene nanocomposite filled with spinel ferrite NiFe$_2$O$_4$ nanoparticles and in-situ thermally-reduced graphene oxide for electromagnetic interference shielding application. Nanomater 9:621–635

Yu W, Chen J, Shang T, Chen L, Gu L, Peng T (2017) Direct Z-scheme g-C$_3$N$_4$/WO$_3$ photocatalyst with atomically defined junction for H$_2$ production. Appl Catal B 219:693–704

Zhan S, Zhou F, Huang N, Yin Y, Wang M, Yang Y, Liu Y (2015) Sonochemical synthesis of Zn$_3$V$_2$O$_7$ (OH)$_2$ (H$_2$O)$_2$ and g-C$_3$N$_4$/ Zn$_3$V$_2$O$_7$ (OH)$_2$ (H$_2$O)$_2$ with high photocatalytic activities. J Mol Catal A Chem 401:41–47

Zhang J-J, Fang S-S, Mei J-Y, Zheng G-P, Zheng X-C, Guan X-X (2018) High-efficiency removal of rhodamine B dye in water using g-C$_3$N$_4$ and TiO$_2$ co-hybridized 3D graphene aerogel composites. Sep Purif Technol 194:96–103

Zhang S, Gu P, Ma R, Luo C, Wen T, Zhao G, Cheng W, Wang X (2019) Recent developments in fabrication and structure regulation of visible-light-driven g-C$_3$N$_4$-based photocatalysts towards water purification: a critical review. Catal Today 335:65–77

Zhang G-L, Pan C-F, Sun Y-H, Wei J-L, Guan D-C, Nan J-M (2021) Synergistic effects of flake-like ZnO/SnFe$_2$O$_4$/nitrogen-doped carbon composites on structural stability and electrochemical behavior for lithium-ion batteries. J Colloid Interface Sci 594:173–185